Investigating Chemical Heterogeneity in Inclusion Population: A multi-variate Population Balance Model Study in Gas-Stirred Ladles

Ashok Kumar Das, Jean-Sébastien Kroll-Rabotin, Thibault Quatravaux, Jean-Pierre Bellot

Investigating Chemical Heterogeneity in Inclusion Population: A multi-variate Population Balance Model Study in Gas-Stirred Ladles

Ashok Das, Jean-Sébastien Kroll-Rabotin, Thibault Quatravaux, and Jean-Pierre Bellot

Institut Jean Lamour, Université de Lorraine, Labex DAMAS, 54000 Nancy, France

September 6, 2023

Abstract

Achieving high mechanical performance in metallic materials requires precise control of the inclusion population, and the treatment of liquid steel in gas-stirred ladles is crucial for inclusion cleanliness in specialty steels. Tracking inclusion properties, such as size, chemical composition, etc. is crucial in modeling of inclusion behavior during liquid metal treatment. A comprehensive multi-variate population balance model (PBM) is developed to track the temporal evolution of the inclusion population inside the ladle. The model is developed by incorporating micro-mechanisms such as aggregation of inclusions, upward sedimentation of inclusions, interception of inclusions by rising bubbles, and capture of inclusions in the slag at the top. The bivariate population balance equation is solved using a weighted finite volume scheme to account for the chemical heterogeneity of inclusions. The simulation results, when applied to an industrial gas-stirred ladle operation, show the efficiency of this modelling approach and offer a way to quantify the respective roles of different mechanisms on inclusion removal rate. Furthermore, the PBM has produced new results for multi-component inclusion systems, including the distribution of inclusions with respect to their chemical components.

Keywords: Non-metallic inclusions, Gas-stirred ladle, Chemical composition, Population balance, Finite volume scheme

1 Introduction

For a conventional steelmaking plant, the molten steel produced in a basic oxygen furnace or electric furnace is poured into a gas-stirred ladle for alloying and refining prior to casting. The deoxidation process occurs at the end of the primary metallurgy when deoxidizers, such as aluminium, silicium,

or calcium, are introduced into the molten steel. This produces an excessive amount of oxide inclusions, which are non-metallic in nature, with their size ranging from nanometers to micrometers. Controlling the amount and extent of these non-metallic inclusions (NMI) is crucial and challenging in producing and recycling high-performance steel. These NMIs are often considered harmful to the quality and lifespan of final products and have detrimental effects on the mechanical and microstructural properties in general [1]. On the contrary, in few situations, the presence of well controlled NMIs inside steel provides nucleation sites to acicular ferrite, which helps in the production of tailored micro-structures [2]. For these reasons, it is crucial to track the temporal evolution of number, mass, size distribution, chemical compositions, and morphology of the inclusion populations throughout the production process.

This work is a development, using a multi-variate population balance modeling (PBM) approach, of the inclusion population in a spatially homogeneous secondary steel ladle process. This work aims at tracking the heterogeneity in chemical compositions of inclusions along with their size distribution, mass, and number evolution, without commenting on the morphology of the inclusions.

2 Description of the process and state of the art

Gas-stirred ladle treatment of liquid metal is a widely used process in secondary steelmaking and is known to be responsible for changes in the inclusion population. An elementary schematic of the liquid steel treatment inside a gas-stirred ladle is illustrated in Fig. 1. The ladle is implanted inside a sealed vessel, which undergoes degasification to remove dissolved gaseous components. Then aluminium, silicium, or calcium are added into the ladle in the form of cored wires for the deoxidation of dissolved oxygen. Additionally, argon gas is injected through one or more porous plugs to achieve thermal and spatial homogeneity and to entrap NMIs by the bubble stream. During this process, the inclusion particles are transported by the turbulent steel flow. Consequently, one can observe the following mechanisms which impact the state of the inclusion population:

- the collision between inclusions, which results in either cluster-like aggregation, or agglomeration if reconstruction of aggregate occurs leading potentially to morphology change [3].
- the attachment of inclusions on the surface of bubbles, which is called the flotation mechanism and several authors have paid research effort for a better understanding and modeling of this mechanism [4, 5]. It is assumed that the entrapped inclusions flow out of the bath with the bubbles.
- the sedimentation of inclusions due to buoyancy forces. Since the density of NMIs is lower than the liquid steel, the inclusions experience an upward motion.
- the capture of inclusions at the top slag layer due to Brownian motion and turbophoretic transport.

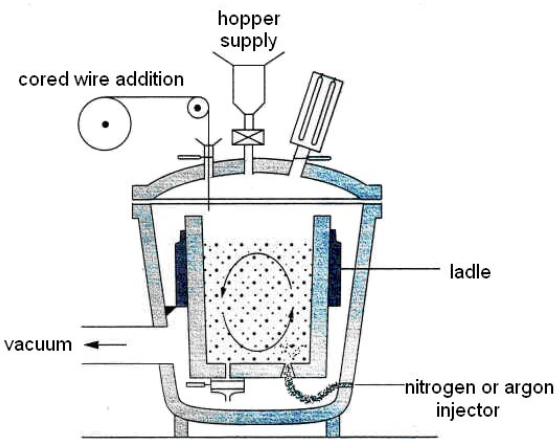

Figure 1: Schematic diagram of the liquid steel ladle refining facility.

Steel ladle modeling has already been the subject of many studies, mainly with the aim of controlling the population of NMI. Until the late '80s, research on inclusion cleanliness was focused on thermodynamic studies aimed to determine the experimental equilibrium slag-metal-inclusion [6]. Since the '90s, the knowledge of thermo-chemical equilibrium has been capitalized on and gave rise to computing software, now widely used in the steelmaking industry to predict the composition of stable phase inclusions [2]. Furthermore, the emergence of CFD has allowed increasingly sophisticated simulations of the multiphase flow in gas-stirred ladles. This type of work, lead by KTH in Stockholm [7] and the University of Urbana-Champaign [8], was considered as a benchmark in this field in the early 2000s. Later on and thanks to the increase in computational power, population balance models (PBM) have been coupled with CFD to track the size distribution of NMIs [2, 9–11]. In 2014, Rimbert et al. [12] developed a reduced order multi-component population balance model to track the NMI population of titanium aluminates in liquid steel. The authors considered nucleation-growth, aggregation, and removal as the fundamental mechanisms of the process and accounted for different chemical components thanks to the coupling with thermodynamic databases. In the same period, a population balance model applied to gas-stirred ladle [13–17] called CIREM, has been developed at IJL and coupled with CFD, to predict the evolution of inclusion size distribution over time. The present work is based on this CIREM[1] software.

On the other hand, another essential aspect of population balance modeling for inclusion removal is the development of precise and efficient numerical methods to solve them. Due to their complex formulation, population balance equations (PBE) are analytically solvable for only a small class of simplified collision kernels. Several techniques are available in the literature to solve PBEs numerically. Some popular methods are sectional methods [18–21], method of moments [22–26], and Monte Carlo method [27, 28]. The Monte Carlo method is a probabilistic method that generates random numbers to obtain statistical approximations of entities under consideration. Conversely, the method of moments is a deterministic approach that formulates a system of algebraic equations that can be solved numerically to obtain different moments of population. Although it is computationally less demanding, it

[1] InterDeposit Digital Number IDDN.FR.001.080025.000.S.P.2021.000.30635

does not solve for the particle density function. Sectional techniques divide the entire domain into smaller cells and directly predict the particle number density function in each class. While sectional methods are computationally more demanding than the method of moments, they yield precise predictions of particle distribution in the population. Additionally, sectional methods are easily adaptable to multi-variate systems, making them a popular choice in the research community.
From the above discussions, it appears that while a few studies were conducted with population balances to model the evolution of inclusions in size, none use multi-variate population balance models and discuss the evolution of the chemical composition of inclusions in gas-stirred ladle. This work investigates the evolution of different chemical components in NMIs and their size distribution with time. Following the work of Kaur et al. [20], a comprehensive multi-variate population balance model is developed by modifying the usual population balance equation (PBE) to simulate the inclusion behavior of a spatially homogeneous gas-stirred steel ladle treatment of liquid steel. The detailed description of the multi-variate model and the solution procedure are presented in Sections 3 and 4. Section 5 concentrates on verifying the developed model and predicting new observations. Final conclusions are summarized in Section 6.

3 Mathematical modeling of inclusion population

The behavior of the inclusion population is investigated by tracking the temporal evolution of the population number density function. The general continuous multi-variate PBE to investigate the homogeneously agitated ladle inclusion population can be written in the following integro-differential form:

$$\frac{\partial n(\vec{v},t)}{\partial t} = \overbrace{\frac{1}{2}\int_{\vec{0}}^{\vec{v}} \beta(\vec{v}-\vec{v'},\vec{v'},t)\, n(\vec{v}-\vec{v'},t)\, n(\vec{v'},t)\,\mathrm{d}\vec{v'}}^{B_{agg}} \underbrace{- n(\vec{v},t)\int_{\vec{0}}^{\vec{\infty}} \beta(\vec{v},\vec{v'},t)\, n(\vec{v'},t)\,\mathrm{d}\vec{v'}}_{D_{agg}} - S(\vec{v}) - C(\vec{v}) - Z_b(\vec{v}) \quad (1)$$

with the following initial condition:

$$n(\vec{v},0) = n_0(\vec{v}) \quad (2)$$

Here, $\vec{v} = (v_1, v_2, \ldots, v_d)$ is the internal property coordinate, where v_r ($r \in \{1 \ldots d\}$) are additive properties of the inclusions. In this work, the internal properties are volume contents of each chemical component in the inclusions so that the total volume of an inclusion of coordinate $\vec{v}$ is $\sum_r v_r$. Together, they define the chemical heterogeneity of the inclusion population. The number density function (NDF) $n(\vec{v},t)$ denotes the number concentration (N) of inclusions per unit of each internal

property at coordinate $\vec{v}$, that is

$$n = \left. \frac{\mathrm{d}^d N}{\prod_{r=1}^{d} (\mathrm{d}v_r)} \right|_{\vec{v}} \tag{3}$$

where d is the number of dimensions of the coordinate vector, that is here the number of chemical components considered in the PBE. The unit of the NDF depends on the dimension of the internal property coordinates. Noting d the number of the chemical components, the SI unit of the NDF $n(\vec{v}, t)$ is $[\#/\mathrm{m}^{3d+3}]$.

The first term in Eq. (1) denotes the rate of change in the NDF with respect to time. In this study, the number density is assumed to be homogeneous in the gas stirred ladle, so that its rate of change is driven by aggregation as well as recovery mechanisms represented as sink terms Z_b, S and C, and does not consider transport in the liquid metal flow.

The first two terms (B_{agg} and D_{agg}) on the right hand side of Eq. (1) denote the birth and death rate of inclusions per unit ladle volume with property coordinates $\vec{v}$ due to the aggregation between inclusions respectively. The function $\beta(\vec{v}, \vec{v'}, t)$ is called the aggregation kernel and denotes the number normalized rate of aggregation events per unit ladle volume between inclusions of chemical nature $\vec{v}$ and $\vec{v'}$ at time t. Furthermore, the aggregation kernel β is considered to be symmetric with its first two arguments, since the collisions between inclusion pairs $(\vec{v}, \vec{v'})$ and $(\vec{v'}, \vec{v})$ are equivalent to each other. Hence, in the collision of two inclusions, the death term (D_{agg}) removes two inclusions, one at coordinate $\vec{v}$ and one at $\vec{v'}$, and the birth term (B_{agg}) creates a new inclusion at $\vec{v} + \vec{v'}$.

The last three terms of PBE (1) are the removal rate of inclusions per unit ladle volume due to the bubble-flotation mechanism (Z_b), sedimentation (S), and deposition at the top boundary layer (C), respectively. The detailed formulation of all these mechanisms is described in the following subsections.

3.1 Aggregation of inclusions

The aggregation mechanism is generally assumed to be a second-order rate process, where inclusions collide and aggregate to form larger inclusions. In a homogeneously agitated steel ladle process, the motion of dispersed inclusions in the liquid metal phase is driven by sedimentation and turbulent transport. Due to the difference in densities between the liquid steel and inclusions ($\rho_p < \rho_l$), inclusions tend to move upwards with a settling velocity that is strongly dependent on inclusion diameter:

$$u_p^{\mathrm{sed}} = \frac{g|\rho_l - \rho_p|}{18\,\mu_l} d_p^2 \tag{4}$$

where the subscripts l and p respectively denote properties of liquid metal and inclusions. Furthermore, ρ denotes density and μ is the dynamic viscosity. Assuming inclusions remain globular, their equivalent diameter can be estimated as the one of a sphere of the same volume as the inclusion.

$$d_p = \frac{6}{\pi} \left(\sum_{r=1}^{d} v_r \right)^{1/3} \tag{5}$$

Consequently, population of inclusions of different sizes (or different densities) have different settling velocities and will thus collide due to their relative velocities. The aggregation kernel due to the sedimentation mechanism, so called the Stokes collision kernel, is derived from the relative settling velocity between two inclusions by calculating its flux through a collision cross section defined so that particles collide when the minimal distance between them is less than the sum of their radii [17].

$$\beta^{\text{sed}}(\vec{v},\vec{v}') = \pi\left(\frac{d_p + d_p'}{2}\right)^2 |u_p^{\text{sed}} - u_p'^{\text{sed}}| \tag{6}$$

Furthermore, the aggregation kernel due to turbulent transport can be obtained from the Zaichik's model [29] and can be presented in a similar form:

$$\beta^{\text{turb}}(\vec{v},\vec{v}') = 4\sqrt{\pi}\left(\frac{d_p + d_p'}{2}\right)^2 \left(U_{\text{in}}^2 + U_{\text{sp}}^2\right)^{1/2} \tag{7}$$

where the corresponding velocity $(U_{\text{in}}^2 + U_{\text{sp}}^2)^{1/2}$ considers two contributions U_{in} and U_{sp} that respectively denote the velocity difference between two particles in a turbulent flow due to their inertia and due to their distance.

Finally, as a first approximation to account for both mechanisms, the inclusion aggregation kernel for the liquid steel ladle process is constructed by adding the aggregation kernels due to sedimentation and to turbulent transport:

$$\beta(\vec{v},\vec{v}',t) = \beta^{\text{sed}}(\vec{v},\vec{v}') + \beta^{\text{turb}}(\vec{v},\vec{v}') \tag{8}$$

3.2 Capture at the free surface

Similarly to aggregation, capture of inclusions at the free surface is driven by the same two mechanims: sedimentation and turbulent transport. The density difference between inclusions and the liquid phase results in the upward sedimentation of inclusions with a velocity expressed in Eq. (4). When particles reach the free surface, they get trapped in the slag layer and are thus recovered from the liquid metal, which is represented by a sink term in the PBM. The inclusion flux depositing at this interface is the product of the sedimentation velocity and the surface area of the free surface. Consequently, the sink term per unit of volume due to the sedimentation, S in Eq. (1), can be written as:

$$S(\vec{v},t) = \frac{u_p^{\text{sed}}\, n(\vec{v},t)\, S_{\text{slag}}}{V_{\text{ladle}}} = \frac{d_p^2|\rho_l - \rho_p|g}{18\mu_l\, H_{\text{ladle}}} n(\vec{v},t) \tag{9}$$

where, H_{ladle} and V_{ladle} are the height and total volume of the ladle, and S_{slag} is the surface area of the free surface at its top.

Moreover, the model for the deposition velocity of inclusions in the boundary layer at the interface with the slag is based on a general law for particle deposition initially developed by Wood et al. [30] that accounts for both turbulent transport (or turbophoresis) and Brownian motion [31]. This deposition velocity depends on the shear velocity u^*, and two dimensionless numbers: the Schmidt number Sc (for Brownian motion) and the particle Stokes number St (for turbophoresis). It is expressed as a

sink term in the PBM in the same way as the sedimentation flux [16, 17], that is:

$$C(\vec{v},t) = \frac{\left(5.7\times10^{-3}\,Sc^{-\frac{2}{3}} + 4.5\times10^{-4}\,St^{2}\right)u^{*}}{H_{\text{ladle}}} n(\vec{v},t) \tag{10}$$

3.3 Flotation

Argon injected at the bottom of the ladle flows to the free surface through the system in the form of gas bubbles. Due to their low wettability in liquid steel, when in contact, inclusions strongly attach to gas bubbles and rise to the surface along with the bubbles. This flotation phenomenon thus also contributes to inclusion recovery from the liquid phase. This recovery mechanism is driven by collision between inclusions and bubbles and follows the same collision dynamics that were considered for aggregation, that is collisions due the relative buoyancy between inclusions and gas bubbles and collisions due to turbulence. Consequently, the outflow rate of inclusions due to the flotation mechanism of bubbles is expressed as:

$$Z_b(\vec{v},t) = \left[E_c\,\beta_b^{\text{sed}} + \beta_b^{\text{turb}}\right] N_b\, n(\vec{v},t) \tag{11}$$

where, N_b denotes the numeral density of bubbles inside the system. Since the objective of this study is to track the inclusion population only, a steady flow rate of argon is considered, resulting in a constant value for N_b.

The collision rate between bubbles and inclusions, due to the sedimentation mechanism, can be written using the same deterministic Stokes collision criterion that was used for aggregation in Eq. (6), but because of the very large size ratio between gas bubbles and inclusions and because of the deformation of rising bubbles, the expression is adjusted with a collision efficiency parameter E_c [32]:

$$\beta_b^{\text{sed}} = \pi\left(\frac{d_b + d_p}{2}\right)^2 |u_b^{\text{sed}} - u_p^{\text{sed}}| \tag{12}$$

where subscript b denotes bubble properties and the efficiency parameter is defined as

$$E_c = \frac{c\,d_p}{d_b} \tag{13}$$

with c is the shape coefficient of the gas bubble. In practice, the value of c is chosen to be 1.7 for spherical cap bubbles and 3 for spherical bubbles [32].

Regarding turbulence driven collision, inclusions are much smaller than the bubbles ($d_p \ll d_b$) and their inertia compared to the bubbles is negligible. Consequently, the Saffman and Turner's collision kernel [33] can be readily applied, leading to the following equation:

$$\beta_b^{\text{turb}} = \sqrt{\frac{8\pi}{15}}\left(\frac{d_b + d_p}{2}\right)^3 \left(\frac{\rho_l \epsilon}{\mu_l}\right)^{1/2} \tag{14}$$

where ϵ is the average dissipation rate of the turbulence.

4 Finite volume scheme

In order to solve and predict the temporal evolution of the inclusion population inside the steel ladle, one needs to solve the multi-variate PBE (1) with rate functions (9), (10) and (11) precisely. The most important task is to solve the multi-variate aggregation mechanism with good accuracy. For this study, the aggregation model is solved using a modified finite volume discretization approach based on the work of Kaur et al. [20]. The details of the finite volume scheme and its utilization in the gas-stirred ladle are discussed in the following subsections.

4.1 Pure batch aggregation

For numerical treatment, it is essential to truncate the domains of integration in a finite range. Let us consider the finite upper limit of the inclusion property coordinates be $\vec{L} = \{L_1, L_2, \ldots, L_d\}$. Then the truncated continuous form of the multi-variate pure batch aggregation PBE is

$$\frac{\partial n(\vec{v},t)}{\partial t} = \frac{1}{2}\int_{\vec{0}}^{\vec{v}} \beta(\vec{v}-\vec{v'},\vec{v'},t)\, n(\vec{v}-\vec{v'},t)\, n(\vec{v'},t)\, \mathrm{d}\vec{v'} - n(\vec{v},t)\int_{\vec{0}}^{\vec{L}} \beta(\vec{v},\vec{v'},t)\, n(\vec{v'},t)\, \mathrm{d}\vec{v'} \quad (15)$$

Now, let us discretize the computation domain $\Lambda = \prod_{r=1}^{d}[0, L_r[$ into $I = \prod_{r=1}^{d} I_r$ number of smaller cells $\lambda_i = \prod_{r=1}^{d}[v_{i_r-1/2}, v_{i_r+1/2}[$, where $i \in 1, 2, \ldots, I$, with the general convention $v_{1_r-1/2} = 0$ and $v_{I_r+1/2} = L_r$ for $r = 1, 2, \ldots, d$. Furthermore, we denote the co-ordinates of the pivot point of the i-th cell as $\vec{v}_i = (v_{i_1}, v_{i_2}, \ldots, v_{i_d})$, where $v_{i_r} = \dfrac{v_{i_r-1/2} + v_{i_r+1/2}}{2}$. A simple schematic of the discretization scheme is illustrated in Fig. 2. The pivot point is considered as the representative of the cell, i.e., all inclusions present inside the cells are concentrated at the pivot point with the following properties (for i-th cell):

- Volume coordinates [m^3]: $\vec{v}_i = (v_{i_1}, v_{i_2}, \ldots, v_{i_d})$.
- Volume of each inclusion [m^3]: $v_i = \sum_{r=1}^{d} v_{i_r}$.
- Number concentration of inclusions [#/m^3]: $N_i = \int_{\lambda_i} n(\vec{v},t)\, \mathrm{d}\vec{v}$.
- Volume concentration of each chemical component r [-]: $V_{i_r} = \int_{\lambda_i} v_r\, n(\vec{v},t)\, \mathrm{d}\vec{v}$.
- Composition coordinates [-]: $\vec{V}_i = (V_{i_1}, V_{i_2}, \ldots, V_{i_d})$.

Several discretization schemes exist in the literature to solve the PBE (15), which are already discussed in the introduction section. The applicability of a numerical method depends on the accuracy in predicting crucial particle properties, such as mass conservation, number evolution, conservation of chemical heterogeneity, etc. In 2017, Kaur et al. [20] proposed a weighted discretization model of PBE (15) in number form, which directly calculates the particle number distribution inside cells and concurrently preserves the time evolution of total number of particles and conserves the total mass of

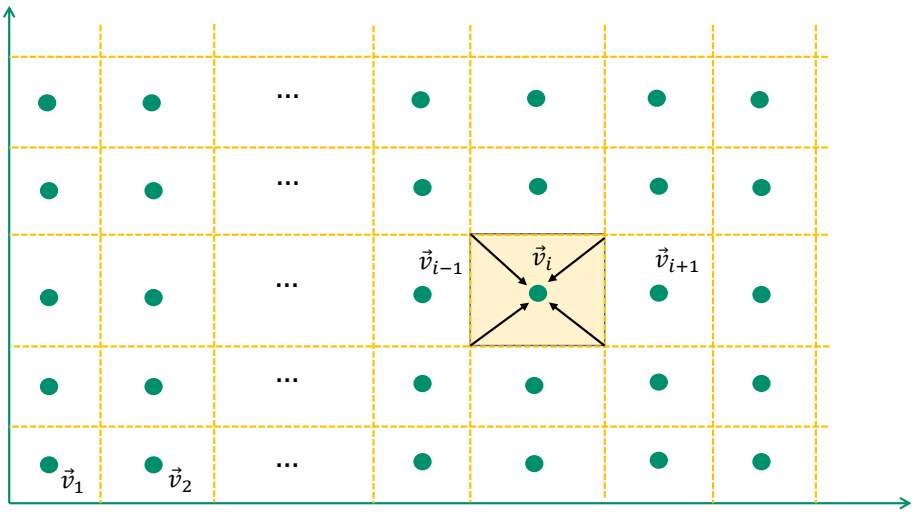

Figure 2: Schematic diagram of the domain discretization.

the particles. However, it was also shown that the scheme does not conserve individual composition masses in general, which is one crucial drawback of the number forms in general. In steelmaking processes, it is critical to track the mass distribution of chemical components and the structural heterogeneity of NMI populations, which are also the main objectives of this study. For this, we use the modified form of PBE (*composition form*) and use a modified version of weighted finite volume scheme of Kaur et al. [20]. The composition form of the continuous PBE can be written by multiplying both sides of PBE (15) with the property coordinate $\vec{v}$ in the following form:

$$\frac{\partial[\vec{v}\,n(\vec{v},t)]}{\partial t} = \frac{\vec{v}}{2}\int_{\vec{0}}^{\vec{v}} \beta(\vec{v}-\vec{v'},\vec{v'},t)\,n(\vec{v}-\vec{v'},t)\,n(\vec{v'},t)\,\mathrm{d}\vec{v'} - \vec{v}\,n(\vec{v},t)\int_{\vec{0}}^{\vec{\infty}} \beta(\vec{v},\vec{v'},t)\,n(\vec{v'},t)\,\mathrm{d}\vec{v'} \quad (16)$$

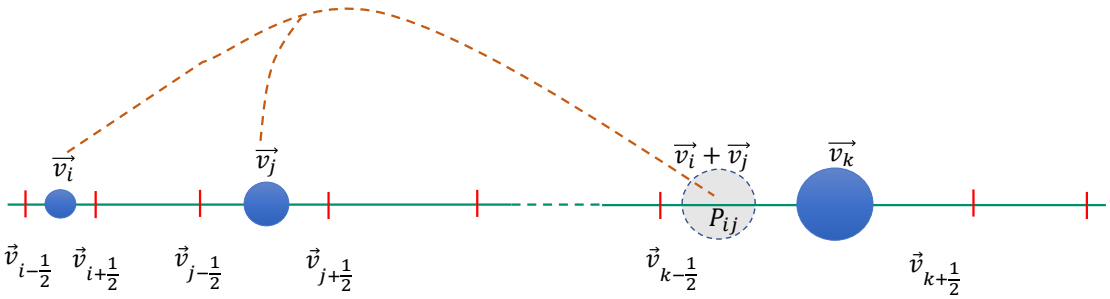

Figure 3: Schematic diagram of the aggregation mechanism to explain the need of weighted FVS.

During aggregation, for unstructured meshing, the aggregate of two inclusions may appear at some non-pivot position of a cell. For example, in Fig. 3, the aggregation event of $\vec{v}_i$ and $\vec{v}_j$ results in the emergence of an inclusion with property $\vec{v}_i + \vec{v}_j$ inside the k-th cell, which is non-identical to the pivot element $\vec{v}_k$. This disrupts moments preservation of the continuous PBE. These issues can be resolved by adding appropriate weight functions while discretizing the composition form of PBE (16) in the

following form:

$$\frac{\mathrm{d}\vec{V}_i}{\mathrm{d}t} = \frac{1}{2} \sum_{(j,k)\in Q_i} \beta_{j,k} \left(\vec{v}_j + \vec{v}_k\right) \frac{\vec{V}_j}{\vec{v}_j} \frac{\vec{V}_k}{\vec{v}_k} w_{j,k} - \sum_{j=0}^{I} \beta_{j,k} \vec{V}_i \frac{\vec{V}_j}{\vec{v}_j} w_{i,j} \tag{17}$$

This is a system of $(I \times d)$ nonlinear ordinary differential equations, which upon solving provides an estimation of component-wise volume of each cell. The set Q_i is the collection of particle pairs, which falls in the i-th cell when aggregated. All the vector multiplication and divisions in the FVS (17) indicate component-wise operations. The corresponding weight functions are

$$w_{i,j} = \begin{cases} \dfrac{\Psi\left(\dfrac{\vec{V}_i}{\vec{v}_i}\right) \Psi\left(\dfrac{\vec{V}_j}{\vec{v}_j}\right)}{2\Psi\left(\dfrac{\vec{V}_i}{\vec{v}_i}\dfrac{\vec{V}_j}{\vec{v}_j}\right) - \Psi\left(\dfrac{\vec{v}_i + \vec{v}_j}{\vec{v}_{l_{ij}}}\dfrac{\vec{V}_i}{\vec{v}_i}\dfrac{\vec{V}_j}{\vec{v}_j}\right)}, & \text{if } \vec{v}_i + \vec{v}_j \leq \vec{v}_I \\ 0, & \text{otherwise.} \end{cases} \tag{18}$$

Here Ψ is a linear arithmetic operator and is used to estimate the number of inclusions in each cell in the following manner:

$$N_i = \Psi\left(\frac{\vec{V}_i}{\vec{v}_i}\right) \tag{19}$$

The formulations (17) and (18) become invalid when dealing with cell pivots that contain zero elements. For instance, if the r-th coordinate of the i-th cell pivot $\vec{v}_i$ is zero, i.e., $v_{i_r} = 0$, then the corresponding volume of chemical component r, denoted by V_{i_r}, is also zero. This happens when the population contains particles that do not contain any amount of some component, such as inclusions of single chemical nature, just after they precipitate and before they interact with other species. As a result, the ratio $\dfrac{V_{i_r}}{v_{i_r}}$ becomes undefined in the expressions (17) and (18). To overcome this issue, we propose an approach to estimate these undefined ratios $\left(\dfrac{V_{i_r}}{v_{i_r}}\right)$ by calculating the average of only the definite ratios $\dfrac{V_{i_k}}{v_{i_k}}$, where $v_{i_k} \neq 0$.

Additionally, in their research article, Kaur et al. [20] utilized the arithmetic mean operator as their choice for Ψ. However, this choice also encounters the same problem of indeterminate ratios mentioned earlier. Moreover, the arithmetic mean operator assigns equal weights to all component coordinates, which can introduce significant inaccuracies when dealing with a wide range of component coordinate values. For instance, consider a bi-component inclusion with volume coordinates (v_{i_1}, v_{i_2}) and composition coordinates (V_{i_1}, V_{i_2}), where $v_{i_1} << v_{i_2}$ and subsequently $V_{i_1} << V_{i_2}$. In this case, the ratio $\dfrac{V_{i_1}}{v_{i_1}}$ will suffer from more rounding off and truncation errors during simulation compared to the other component ratio $\dfrac{V_{i_2}}{v_{i_2}}$. The equal weighted arithmetic mean operator will exacerbate these numerical errors. To address this issue, we propose prioritizing the components based on their com-

position coordinate proportions, which mitigates the impact of numerical errors and indeterminate factors. We present our modified formulation as follows:

$$N_i = \Psi\left(\frac{\vec{V}_i}{\vec{v}_i}\right) = \frac{\sum_{k=1}^{d} V_{i_k}}{\sum_{k=1}^{d} v_{i_k}} = \sum_{k=1}^{d}\left(\frac{v_{i_k}}{\sum_{r=1}^{d} v_{i_r}}\right)\frac{V_{i_k}}{v_{i_k}} \tag{20}$$

This modification resolves the occurrence of indeterminate ratios and incorporates weights based on the volume coordinate proportions, ensuring numerical stability.

Finally, it is also mathematically demonstrated [20] that the Finite Volume Scheme given by Eq. (17) conserves the total mass of each chemical composition and preserves the temporal evolution of the total number for a batch aggregation process. This is due to the fact that the FVS approach accurately accounts for the production and consumption rates of chemical species, as well as their fluxes through the boundaries of each cell. This enables the scheme to accurately predict the behavior of the system over time, while ensuring that the overall mass of each chemical composition remains constant.

4.2 Population balance model for the inclusion population inside ladle

In order to solve the PBE (1) corresponding to the inclusion population (including all mechanisms) numerically, we can follow a similar line to the previous description and obtain the following discrete formulation as

$$\begin{aligned}\frac{\mathrm{d}\vec{V}_i}{\mathrm{d}t} &= \frac{1}{2}\sum_{(j,k)\in Q_i}\beta_{j,k}\left(\vec{v}_j+\vec{v}_k\right)\frac{\vec{V}_j}{\vec{v}_j}\frac{\vec{V}_k}{\vec{v}_k}\,w_{j,k} - \sum_{j=0}^{I}\beta_{j,k}\,\vec{V}_i\,\frac{\vec{V}_j}{\vec{v}_j}\,w_{i,j} \\ &- \left[\left(E_c\,\beta_b^{\text{sed}}+\beta_b^{\text{turb}}\right)N_b - \frac{d_i^2|\rho_l-\rho_p|g}{18\,\mu_l\,H_{ladle}} - \frac{\left(5.7\times10^{-3}\,Sc^{-\frac{2}{3}}+4.5\times10^{-4}\,\tau_p^2\right)u^*}{H_{ladle}}\right]\vec{V}_i\end{aligned} \tag{21}$$

with the similar weight functions as Eq. (18). It is important to note that the additional sink terms in Eq. (21) are expressed at pivot points and only influence the rate of change of the death term in $\vec{V}_i$. They do not introduce or remove data at the pivot locations, nor do they necessitate any special treatments.

5 Results and discussion

This section is devoted to establishing the accuracy and efficiency of the proposed multi-variate PBM Eq. (21) of the inclusion population. Consequently, this section is divided into three subsections. Subsection 5.1 discusses the selection of optimal level of discretization by comparing the proposed model predictions against results available in the literature. Due to the unavailability of multi-variate models of inclusions in gas-stirred ladles in the literature, the univariate CIREM-0D model of Bellot et al. [17] is taken as reference case. In this study, the authors developed a univariate PBM of the gas-stirred ladle process to track the inclusion population. The volume of inclusion particles was considered the only internal property coordinate, and no effect of chemical heterogeneity was considered. A typical

60 t stirred ladle system with high stirring intensity was simulated with a total inclusion content of 0.176 kg/m^3. Further, it was considered that the inclusion particles are homogeneously distributed in the system with an initial log-normal size distribution. The initial volume density distribution of the inclusion population in the ladle is illustrated in Fig. 4. To provide a clear understanding, the mathematical formulation for calculating the volume density function for the entire ladle system is presented below:

$$\Phi(\vec{v}, t) = \sum_{r=1}^{d} v_r \, n(\vec{v}, t) \, V_{\text{ladle}} \tag{22}$$

This volume density function (Φ) is a dimensionless quantity for univariate distributions, is the inverse of a volume [m^{-3}] for bivariate distributions. In the following sections, for the purpose of verification, the multi-variate population densities have been converted during post-processing into their univariate form based on inclusion volume that enables the calculation and comparison of the volume density distributions. Finally, the reference case, CIREM-0D, solves the univariate PBM using the Cell Average Technique (CAT) of Kumar et al. [18].

Subsection 5.2 verifies the developmental accuracy and applicability of the proposed PBM against CIREM-0D results for different test cases. Finally, some new predictions for a bivariate system, i.e., for inclusion particles with different chemical components are presented and discussed in Subsection 5.3.

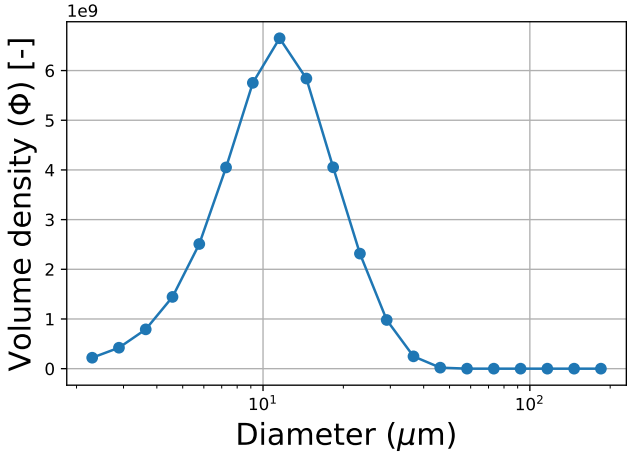

Figure 4: Initial volume density distribution of the inclusion population.

5.1 Selection of discretization level

To ensure accurate and efficient calculations, the adequate level of discretization is assessed. Bellot et al. [17] discretized the computational domain into 20 geometric grid points and solved it using the CAT. As a first step, to facilitate comparison, the proposed multi-variate model is restricted to univariate case and solved with the same discretization up to a process time of 300 s. Fig. 5 displays the comparison of the final volume density distribution obtained from the weighted FVS and the CAT [17]. Although both methods produce similar trends for the volume density distribution, they are not equivalent in nature. Therefore, the accuracy of the discretization levels was examined, and

Fig. 5 further illustrates the comparison of the volume density distributions obtained for 40 grid points, which shows good agreement between the CAT and FVS results.

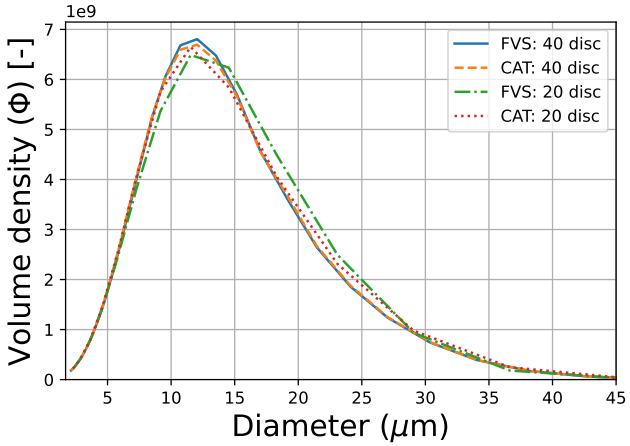

Figure 5: Comparison of volume density distribution at 300 s for different discretization levels.

To further evaluate the appropriate level of discretization for the FVS model, L^1 and L^2 errors [34] are calculated as well as the computer simulation time for different numbers of cells. The results from the CAT with 60 grid points are chosen as the reference case and compared to other schemes and different numbers of cells. The results are tabulated in Table 1. The error values decrease as the number of pivot points increases and show comparable results for 40 cells. Interestingly, while the computer simulation time for the CAT implementation rapidly increases as the grid points increase, the FVS simulation time remains within control for larger grid numbers.

Table 1: Error and simulation time.

Method	# of pivots	L^1 Error	L^2 Error	Simulation time [s]
CAT	20	0.031	0.014	0.298
	40	0.006	0.003	0.378
	60	–	–	19.586
FVS	20	0.107	0.047	0.095
	40	0.0112	0.005	0.170
	60	0.008	0.003	0.386

The accuracy of the new PBM with weighted FVS and 40 grid points is further substantiated by plotting the frequency of different particulate mechanisms at 300 s. During the process, inclusions are continuously eliminated from the system due to mechanisms such as flotation (capture by bubbles), sedimentation, and deposition at the top slag layer. The effect of all these mechanisms and their elimination rates, computed from the new FVS model and CAT model, are plotted in Figures 6a and 6b. The resulting figures shows that the proposed PBM and 1D FVS reproduce CIREM-0D results with great precision. Additionally, it can be observed that the aggregation mechanism plays a dominant role compared to other mechanisms such as flotation, sedimentation, and capture at the top slag, respectively by 1, 3, and 5 orders of magnitude approximately (see Fig. 6a). The signs (-) and

(+) for the aggregation mechanism indicate the net reduction or production of particles of each size class that is calculated using the following equation:

$$F_{agg}(i) = \int_{V_{ladle}} [B_{agg}(i) - D_{agg}(i)] \, \mathrm{d}\mathcal{V} \tag{23}$$

Moreover, the temporal evolution of the inclusion elimination rates due to different removal mechanisms are compared on Fig. 6b that illustrates excellent agreement between the results of CAT and FVS. Since the average inclusion size increases with time and all the elimination rates are highly dependent on inclusion size, the elimination rates for all mechanisms also increase with time. This phenomenon is correctly portrayed in Fig. 6b. Additionally, the elimination rate of the flotation mechanism is higher than the sedimentation and deposition mechanisms by orders of almost 10 and 10^3, respectively. This analysis confirms the ability of reproduction of the proposed PBM against the univariate CIREM-0D results [17]. These thorough investigations of the accuracy and efficiency of the developed population balance model show that the univariate version of the proposed model provide reliable and efficient results for 40 geometrically distributed cells.

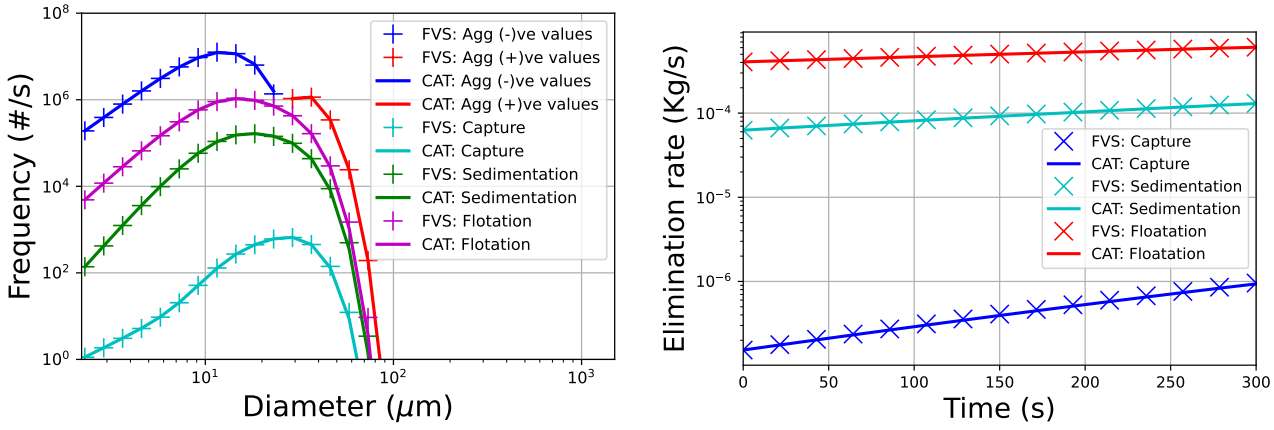

(a) (b)

Figure 6: Comparison of (a) frequency of mechanisms after 300 s as a function of inclusion size and (b) temporal evolution of elimination rates due to different recovery mechanisms.

5.2 Verification of the proposed PBM

As discussed earlier, the model and results of the CIREM-0D program from the work of Bellot et al. [17] were considered for verification purpose. In order to check the applicability of multi-variate population balance model (21) with the weighted FVS (17) against CIREM-0D results, three different setups are considered.

The first setup is the one discussed in the former subsection, in which the multi-variate setup is restricted to a univariate model with inclusion volume as the internal coordinate. The other two setups consider bivariate populations, i.e., the inclusions are made of two different chemical components C_1 and C_2. The corresponding internal coordinate of the inclusions is (v_1, v_2), which means an inclusion with v_1 and v_2 volumes of composition C_1 and C_2, respectively. For a comparative analysis with the

CIREM-0D, the same initial particle size distribution as CIREM is considered and distributed among both components as:

- **Case 50-50**: 50% pure C_1 inclusions + 50% pure C_2 inclusions.
- **Case 80-20**: 80% pure C_1 inclusions + 20% pure C_2 inclusions.

So-called pure inclusions are inclusions with one of their internal volume coordinate equal to zero. Furthermore, it is essential to note that if we project these cases to one-dimension, i.e. the chemical nature of the initial inclusions is not considered, only their volume is, these two test cases are equivalent to the univariate case. For this reason, cases 50-50 and 80-20 can be viewed as direct generalization of CIREM-0D to bivariate systems. With these setups, all the cases are solved for a 300 s of process time to check the accuracy and efficiency of the developed PBM.

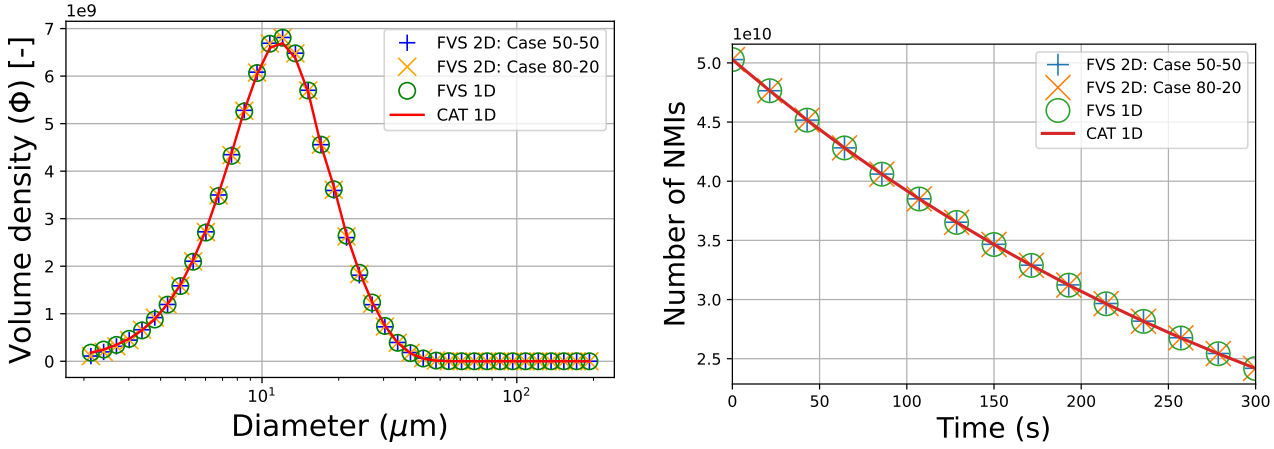

(a) (b)

Figure 7: Comparison of (a) volume density distribution at 300 s as a function of inclusion diameter and (b) temporal evolution of number of inclusions.

The comparison of the final volume density distribution obtained from the proposed model with the weighted FVS solver for univariate and bivariate (50-50 and 80-20) cases and univariate CIREM with CAT solver are illustrated in Fig. 7a. To ease comparison, the density distributions for bivariate cases are plotted for the total volume of inclusions as a function of inclusion diameter. The figure clearly portrays excellent agreement between the univariate CIREM-0D results and the proposed PBM predictions for both univariate and bivariate cases. The temporal evolution of the total number of inclusions in the system is also presented in Fig. 7b. This figure shows that the reduction rate of total inclusion number for both cases 50-50 and 80-20 are precisely in line with the univariate results of CIREM (CAT) and FVS. This is due to the simple fact that both bivariate cases are just multivariate extensions of the univariate system, and the developed multi-variate FVS model is accurate in predicting this trend.

Similarly, the temporal evolution of the total mass of inclusions in the ladle is exhibited in Fig. 8a, which displays consistent predictions between all simulation cases. Furthermore, the temporal evolution of total masses of individual chemical components for both bivariate cases is illustrated in Fig. 8b.

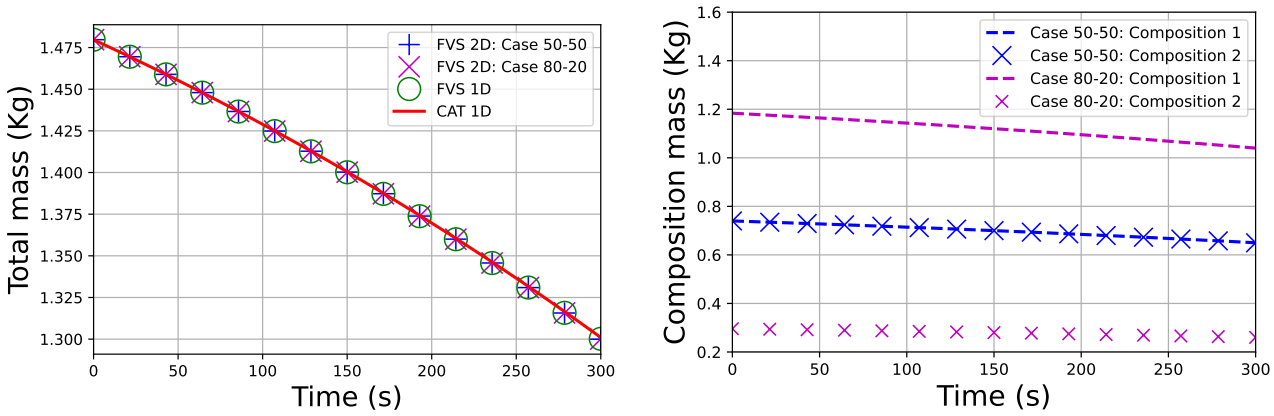

(a) (b)

Figure 8: Comparison of (a) volume density distribution at 300 s as a function of inclusion diameter and (b) temporal evolution of number of inclusions.

Both figures clearly illustrate mass loss of both chemical components due to the sink terms such as sedimentation, flotation, and deposition at the top slag layer due to turbulent transport. Additionally, since sink terms only depend on the inclusion volume, not on their chemical composition, the masses of each chemical component keep their initial ratio (50:50 and 80:20) during the whole simulation for both bivariate cases (see Fig. 8b). Furthermore, to prove that the mass reduction of NMIs is only due to the sink mechanisms and not due to the numerical diffusion in the developed weighted FVS, an additional pure aggregation process has been simulated by turning off all the sink terms. The corresponding evolution of mass of all inclusions and their compositions for both bivariate cases is illustrated in Figures 9a and 9b. These figures prove that the weighted FVS model of aggregation accurately conserves the masses of all individual components along with the total mass of inclusions.

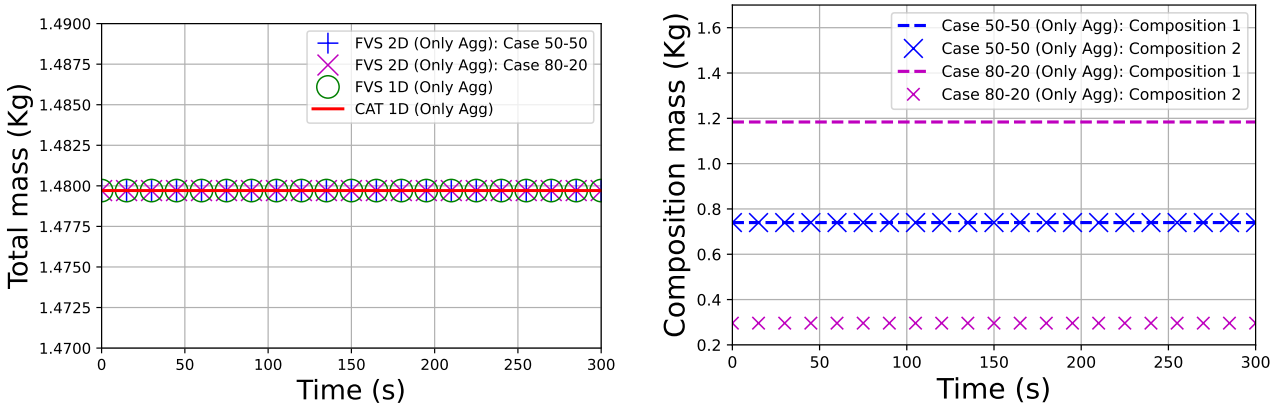

(a) (b)

Figure 9: Comparison of evolution of total chemical compositions: (a) case 50-50 (b) case 80-20.

5.3 Predictions for bivariate systems

This section presents and analyzes new predictions corresponding to the previously discussed bivariate cases. Specifically, cases 50-50 and 80-20 were simulated for a longer period of 800 s to show the

effects of initial chemical composition and size distribution on the final distribution. The temporal evolution of the volume density distributions of mixed inclusions and of pure inclusions for both cases are illustrated in Figures 10 and 11.

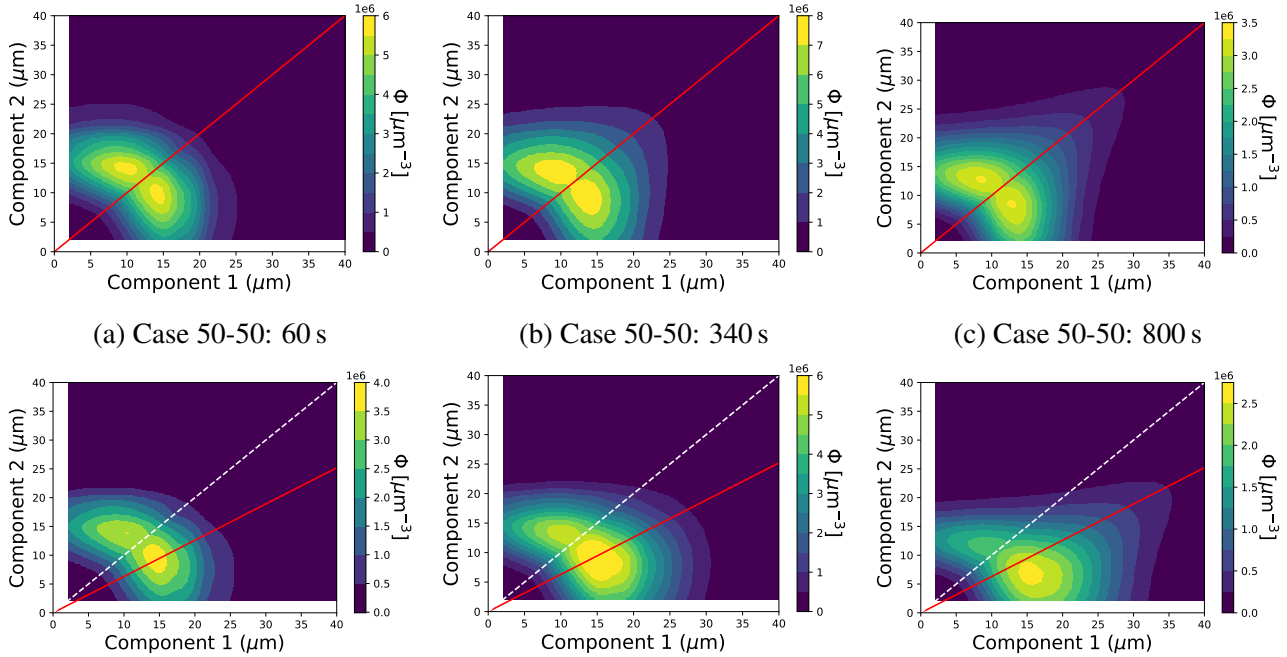

(a) Case 50-50: 60 s (b) Case 50-50: 340 s (c) Case 50-50: 800 s

(d) Case 80-20: 60 s (e) Case 80-20: 340 s (f) Case 80-20: 800 s

Figure 10: Temporal evolution of volume density distributions at different time instances.

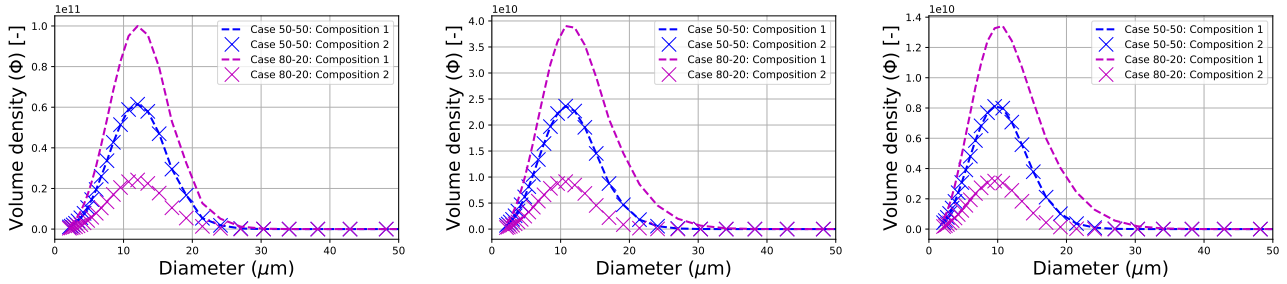

(a) 60 s (b) 340 s (c) 800 s

Figure 11: Temporal evolution of volume density distributions of inclusions with pure compositions at different times.

Case 50-50 starts with equal masses of pure compositions C_1 and C_2 which follow a log-normal distribution in size. Since no specific attraction rules were considered for the composition of inclusions during collision, Fig. 10(a), (b), and (c) exhibit symmetric trends. The results demonstrate that the size of inclusions grows with time, and most inclusions concentrate on the region where NMIs are composed of equal amounts of both compositions. Since the total volume of an inclusion i is $v_i = v_{i_1} + v_{i_2}$, the biggest inclusions are in the top right hand corner of the plots in Fig. 10. The iso-size lines, which indicate inclusions of the same size, are perpendicular to the red line representing the 50-50 composition. The largest aggregates in the distribution are aligned with the 50-50 line. However, for smaller sizes, the distribution exhibits two symmetric peaks. One possible explanation

for this observation is that due to starting with solely pure inclusions, a significant number of pure inclusions persist, especially during the early stages, and most aggregation events involve pure inclusion. Among these aggregation events, only the aggregation between two pure inclusions of distinct components and the same size result in exactly 50-50 aggregates. As a result, the majority of aggregation events lead to non 50-50 aggregates. In contrast, for larger aggregates that are result of successive aggregation steps, this effect vanishes, and their composition resembles the average composition of the initial population.

Case 80-20 yields non-symmetric pattern of the volume density, as depicted in Fig. 10(d), (e), and (f). The peak of the distribution continuously shifts towards the right hand side as time progresses and approaches the red line, which represents inclusions composed of 80% composition C_1 and 20% composition C_2. This is due to starting with 80% C_1 inclusions, leading to a higher occurrence of aggregation between pure C_1 inclusions. The chemical components preserve their initial ratios during the process simulation. Even after 800s, the ratio of the mass of C_1 to the total mass of C_1 and C_2 is still 0.799. The slight decrease in this ratio is due to the transient evolution of inclusion population, where larger aggregates that are more effectively removed tend to contain slightly more C_1 than C_2, as illustrated in Fig. 10(e), but this effect remains very limited. After multiple aggregations, the ridge line of the volume distribution approaches the 80-20 (red) line for the largest aggregates. However, the peak of the distribution surpasses the 80-20 line and corresponds to a composition that is closer to 95% C_1-5% C_2, as shown in Fig. 10(d). This behavior can be explained in the same way as in case 50-50.

The effect of removal of inclusions is visible in Fig. 11, which displays the volume density of pure inclusions, that correspond to the axes of the distributions shown in Fig. 10. In both cases, the peak of the size distributions gradually shifts towards smaller sizes over time. Although this shift is subtle, the total volume of pure inclusions decreases significantly, as evidenced by the evolving vertical scales in Fig. 11(a), (b), and (c). These observations confirm the dominance of aggregation over other removal mechanisms, as also observed in Fig. 6a.

Furthermore, to substantiate the occurrence of aggregation and other removal mechanisms, mass percentages of inclusions with different chemical natures are illustrated in Fig. 12. Three distinct chemical compositions are tracked: pure inclusions (either C_1 or C_2), and inclusions composed of 50%$\pm$3% and 80%$\pm$3% of C_1. The mass percentage of pure NMIs only decreases over time due to both aggregation and removal mechanisms: pure NMIs aggregating with any other composition produce non-pure NMI aggregates. Additionally, we observe that the percentage of pure non-mixed inclusions decreases at a faster rate in the case 50-50 compared to the case 80-20. This can be attributed to the fact that case 80-20 starts with 80% pure C_1 inclusions, resulting in more aggregation between pure C_1 inclusions that produce pure C_1 aggregates. In contrast, case 50-50 has an equal presence of both pure C_1 and C_2 inclusions, making the system more likely to create aggregates with mixed chemical nature. Furthermore, in line with the composition of the initial populations, we observe a rapid increase in the population of mixed inclusions consisting of 50% C_1 and 80% C_1 for the cases 50-50 and 80-20, respectively.

The above-discussed examples make it clear that the developed PBM for inclusions in a gas-stirred

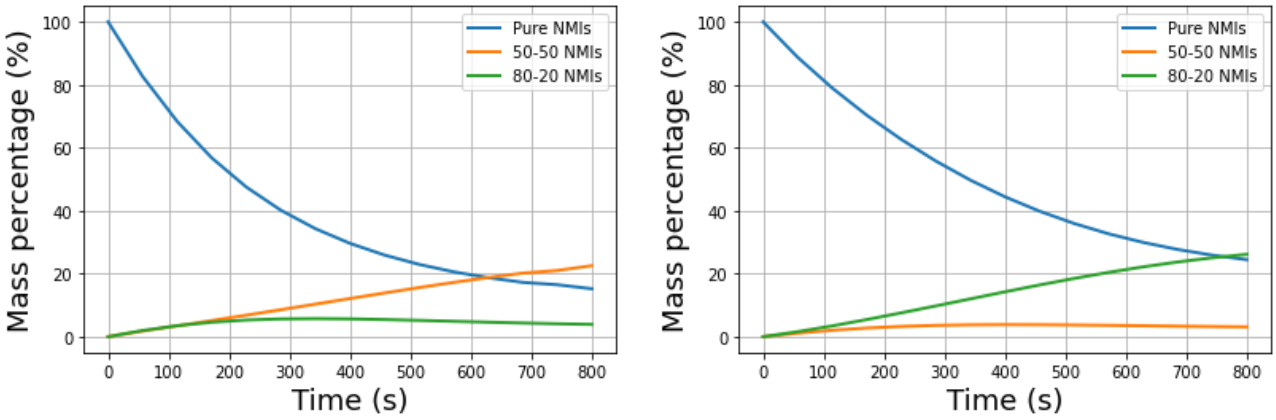

(a) Case 50-50

(b) Case 80-20

Figure 12: Temporal evolution of mass percentage of inclusions with different chemical compositions.

ladle is able to capture the evolution of univariate and multi-variate inclusion populations in steel ladle refining processes. The model successfully tracks the changes in chemical composition of inclusions and effectively represents these transformations in the size distribution. This demonstrates the potential and applicability of multi-variate population balance modeling in steelmaking processes. Moreover, beyond applicability of the method for inclusions in steelmaking processes, these results provide valuable insights into the characteristics and evolution of inclusion populations over time. Particularly notable is the observation that while the largest aggregates contain both components and reflect the initial proportion of the two components, the peak of the distribution does not. This is due to the fact that even after 800 s of treatment, pure inclusions have not fully disappeared, and the resulting population is a balance between production of new mixed aggregates and removal of large aggregates. Because inclusion removal is efficient for larger inclusions, even to the point that it is even visible on pure inclusion size distributions, there is no wide gap in size between mixed aggregates resulting from the combination of pure inclusions and the biggest inclusions. Most size classes are highly sensitive to the initial size distributions of pure inclusions, and only the largest aggregates accurately reflect the ratio of chemical composition among the initial populations. Inclusion populations after 300 s, and even 800 s, are thus still strongly influenced by the initial conditions. Therefore, to effectively capture the behavior of inclusions in a steel ladle, the inclusion population cannot be approximated as a homogeneously mixed particle population. A full multi-variate representation is required, which justifies the development of the presented population balance method and its application to steelmaking ladle processes.

6 Conclusions

A comprehensive multi-variate population balance model of the homogeneous gas-stirred ladle process is presented to track the temporal evolution of the inclusion population. This is the first application of multi-variate population balance to steel ladle refining. To achieve this, an extension of an existing finite volume scheme is presented to resolve the multivariate PBM, enabling the consideration

of particles composed of a single component.
The physical mechanisms governing NMI behavior in a steel ladle have been implemented in this extended finite volume scheme, and the predictions of this model have been validated against results for univariate populations produced with the state-of-the-art simulation software CIREM.
While focusing on the methodological aspects, this investigation lead to interesting preliminary findings regarding inclusions in a steel ladle. Even without considering the impact of the chemical nature of inclusions on their aggregation kinetics, heterogeneity from the initial distribution induce long term heterogeneity of inclusion population, even after prolonged processing when the total mass of inclusions has significantly decreased. Inclusions are continuously removed while aggregation occurs, and due to this fundamentally transient behavior in the ladle, predicting heterogeneity in the final population becomes challenging. Most inclusions are multi-component, but the ratio of each component evolves within the size distribution and over time, and the prevalent classes of inclusions in the final distribution do not reflect the chemical composition of the initial pure populations.
Real inclusions (such as solid fractal-shaped alumina aggregating with calcium oxides) can form phases of different physical nature (such as globular calcium aluminates). To account for such physics in the model, inclusion behaviour must be related to their chemical composition. Inclusions also interact with the liquid phase, and their growth, dissolution, or chemical composition evolves with the composition of the carrying liquid. Furthermore, the chemical composition of inclusions can affect their propensity to aggregate, as different affinities between components come into play. Although it is hard to feed multi-variate population balances of inclusions in steel ladle with physical models to relate their change in behavior to their chemical evolution, these initial findings show that this is a necessary step to improve predictions, since the inclusion population never reaches an equilibrium state where inclusions could be assumed to share most of their chemical and mechanical properties. So far, the scientific literature remains sparse on interaction models between inclusions and their impact on the temporal evolution of inclusion populations. This is a major point to address in order to improve the understanding, modeling, and eventual optimization of steelmaking processes.

Acknowledgement

The authors gratefully acknowledge the financial support provided by Labex DAMAS, University of Lorraine.

References

[1] J. Guan, L. Wang, C. Zhang, X. Ma, Effects of non-metallic inclusions on the crack propagation in bearing steel, Tribology International 106 (2017) 123–131.

[2] M. A. Van Ende, M. Guo, E. Zinngrebe, B. Blanpain, I. H. Jung, Evolution of non-metallic inclusions in secondary steelmaking: Learning from inclusion size distributions, ISIJ international 53 (11) (2013) 1974–1982.

[3] F. Gruy, Population balance for aggregation coupled with morphology changes, Colloids and Surfaces A: Physicochemical and Engineering Aspects 374 (1-3) (2011) 69–76.

[4] L. Zhang, S. Taniguchi, Fundamentals of inclusion removal from liquid steel by bubble flotation, International materials reviews 45 (2) (2000) 59–82.

[5] S. T. Johansen, S. Graadahl, T. F. Hagelien, Entrainment of inclusions from the dross in stirred reactors for melt treatment, Applied Mathematical Modelling 28 (1) (2004) 63–77.

[6] H. Gaye, C. Gatellier, M. Nadif, P. Riboud, J. Saleil, M. Faral, Réaction métal-laitier et contrôle de la composition des inclusions résiduelles en métallurgie secondaire, Revue de métallurgie (Paris) 84 (11) (1987) 759–771.

[7] M. Hallberg, P. Jönsson, T. Jonsson, R. Eriksson, Process model of inclusion separation in a stirred steel ladle, Scandinavian journal of metallurgy 34 (1) (2005) 41–56.

[8] L. Zhang, B. G. Thomas, State of the art in evaluation and control of steel cleanliness, ISIJ international 43 (3) (2003) 271–291.

[9] H. Ling, L. Zhang, H. Li, Mathematical modeling on the growth and removal of non-metallic inclusions in the molten steel in a two-strand continuous casting tundish, Metallurgical and Materials Transactions B 47 (2016) 2991–3012.

[10] E. I. Castro-Cedeno, A. Jardy, B. Boissiere, J. Lehmann, P. Gardin, A. Carré, S. Gerardin, J. P. Bellot, Numerical simulation of modification of non-metallic inclusions by calcium treatment in the argon-stirred ladle, Metallurgical Research & Technology 116 (5) (2019) 515.

[11] L. Li, Z. Liu, B. Li, H. Matsuura, F. Tsukihashi, Water model and cfd-pbm coupled model of gas-liquid-slag three-phase flow in ladle metallurgy, ISIJ International 55 (7) (2015) 1337–1346.

[12] N. Rimbert, L. Claudotte, P. Gardin, J. Lehmann, Modeling the dynamics of precipitation and agglomeration of oxide inclusions in liquid steel, Industrial & Engineering Chemistry Research 53 (20) (2014) 8630–8639.

[13] J.-P. Bellot, N. Rimbert, S. Hans, A. Jardy, Comparison of the class method (CM) and the quadrature method of moments (QMOM) for solving the population balance equation in a 3D liquid steel ladle reactor, in: 8th International Conference on Multiphase Flow, ICMF, Jeju, Korea, 2013, 722.

[14] J.-P. Bellot, A. Bansal, P. Chapelle, E. Waz, Y. Delannoy, P. Lebrun, Agglomeration and transport of a population of oxide inclusions in an aluminum induction furnace, in: 9th International Conference on Multiphase Flow, ICMF, Florence, Italy, 2016, 139.

[15] J. P. Bellot, J. S. Kroll-Rabotin, M. Gisselbrecht, M. Joishi, A. Saxena, S. Sanders, A. Jardy, Toward better control of inclusion cleanliness in a gas stirred ladle using multiscale numerical modeling, Materials 11 (7) (2018) 1179.

[16] V. De Felice, I. L. A. Daoud, B. Dussoubs, A. Jardy, J. P. Bellot, Numerical modelling of inclusion behaviour in a gas-stirred ladle, ISIJ international 52 (7) (2012) 1273–1280.

[17] J. P. Bellot, V. De Felice, B. Dussoubs, A. Jardy, S. Hans, Coupling of CFD and PBE calculations to simulate the behavior of an inclusion population in a gas-stirring ladle, Metallurgical and Materials Transactions B 45 (1) (2014) 13–21.

[18] J. Kumar, M. Peglow, G. Warnecke, S. Heinrich, L. Mörl, Improved accuracy and convergence of discretized population balance for aggregation: The cell average technique, Chemical Engineering Science 61 (10) (2006) 3327–3342.

[19] S. Rigopoulos, A. G. Jones, Finite-element scheme for solution of the dynamic population balance equation, AIChE Journal 49 (5) (2003) 1127–1139.

[20] G. Kaur, J. Kumar, S. Heinrich, A weighted finite volume scheme for multivariate aggregation population balance equation, Computers & Chemical Engineering 101 (2017) 1–10.

[21] M. Singh, New finite volume approach for multidimensional smoluchowski equation on nonuniform grids, Studies in Applied Mathematics 147 (3) (2021) 955–977.

[22] M. Attarakih, M. Jaradat, C. Drumm, H. Bart, S. Tiwari, V. Sharma, J. Kuhnert, A. Klar, A multivariate sectional quadrature method of moments for the solution of the population balance equation, Computer Aided Chemical Engineering 28 (2010) 1551–1556.

[23] A. Buffo, M. Vanni, D. L. Marchisio, R. O. Fox, Multivariate quadrature-based moments methods for turbulent polydisperse gas-liquid systems, International Journal of Multiphase Flow 50 (2013) 41–-57.

[24] R. Fox, Bivariate direct quadrature method of moments for coagulation and sintering of particle populations, Journal of Aerosol Science 37 (11) (2006) 1562–1580.

[25] K. Wang, S. Yu, W. Peng, Extended log-normal method of moments for solving the population balance equation for brownian coagulation, Aerosol Science and Technology 53 (3) (2019) 332–343.

[26] R. G. Patel, O. Desjardins, R. O. Fox, Three-dimensional conditional hyperbolic quadrature method of moments, Journal of Computational Physics: X 1 (2019) 100006.

[27] A. Das, J. Kumar, Population balance modeling of volume and time dependent spray fluidized bed aggregation kernel using monte carlo simulation results, Applied Mathematical Modelling 92 (2021) 748–769.

[28] Y. Lin, K. Lee, T. Matsoukas, Solution of the population balance equation using constant-number monte carlo, Chemical Engineering Science 57 (12) (2002) 2241–2252.

[29] L. I. Zaichik, O. Simonin, V. M. Alipchenkov, Turbulent collision rates of arbitrary-density particles, International Journal of Heat and Mass Transfer 53 (9) (2010) 1613–1620.

[30] N. Wood, A simple method for the calculation of turbulent deposition to smooth and rough surfaces, Journal of aerosol Science 12 (3) (1981) 275–290.

[31] P. Ni, L. T. I. Jonsson, M. Ersson, P. G. Jönsson, On the deposition of particles in liquid metals onto vertical ceramic walls, International Journal of Multiphase Flow 62 (2014) 152–160.

[32] V. Sarrot, P. Guiraud, D. Legendre, Determination of the collision frequency between bubbles and particles in flotation, Chemical Engineering Science 60 (22) (2005) 6107–6117.

[33] P. G. Saffman, J. S. Turner, On the collision of drops in turbulent clouds, Journal of Fluid Mechanics 1 (1) (1956) 16–30.

[34] A. Das, S. Bhoi, D. Sarkar, J. Kumar, Sonofragmentation of rectangular plate-like crystals: Bivariate population balance modeling and experimental validation, Crystal Growth & Design 20 (8) (2020) 5424–5434.